Active Control of Interconversion of Spin and Orbital Angular Momentum of Light by a Scattering System

Zhengyang Mao,[1,‡] Haigang Liu,[1,*,‡] and Xianfeng Chen[1,2,3,†]

[1] *State Key Laboratory of Advanced Optical Communication Systems and Networks, School of Physics and Astronomy, Shanghai Jiao Tong University, Shanghai 200240, China*

[2] *Shanghai Research Center for Quantum Sciences, Shanghai 201315, China*

[3] *Collaborative Innovation Center of Light Manipulations and Applications, Shandong Normal University, Jinan 250358, China*

(Received 20 March 2022; revised 31 May 2022; accepted 13 July 2022; published 23 August 2022)

The conversion between spin and orbital angular momentum plays a crucial role in modern science and has a wide range of applications in optical multistate magnetization, optical micromanipulation, classical and quantum optical communications. However, it becomes difficult in many complex environments due to the inherent scattering effect. Here, we experimentally demonstrate the active control of spin and orbital angular-momentum conversion of light by a scattering system. We obtain significant optimization results and prove that the angular-momentum conversion process in scattering medium is tunable and flexible. Our work opens the door for high-dimensional optical information exchange in complex circumstance and paves the way for applications of optical angular momentum in optical communication.

DOI: 10.1103/PhysRevApplied.18.024061

I. INTRODUCTION

Angular momentum is one of the most fundamental and vital properties of physical particles, which can be divided into spin angular momentum (SAM) [1,2] and orbital angular momentum (OAM) [3–5]. In the last few years, both optical SAM and OAM have proven extremely useful in various fields [1–5]. When the circularly polarized light carrying SAM interacts with the medium, SAM of light will change and therefore trigger the optical rotation effect, which is universally applied in the manipulation of particles and biological cells [6–8]. Since Allen found that vortex beam carries OAM in 1992 [3], it has been proved to have wide applications in both classical and quantum areas [9,10], such as optical microfabrication [11–13], micromanipulation [14–21], OAM entanglement [22–25], and superresolution optical imaging [26]. More compelling and attractive, the optical communication capacity could be increased to another level by using infinite eigenstates of vortex beam as information carriers [27–30].

Recently, there has been enormous interest in the angular-momentum conversion when the light interacts with matter [31,32]. Of note, the conversion between SAM and OAM is essentially the coupling between different degrees of freedom of light field [9]. It breaks through the limitation in traditional optics that different angular momentum can only be adjusted individually. Actually, the angular-momentum conversion is ubiquitous in various kinds of optical processes [33]. The coupling between different angular momentums has been proved to be available in the optical control of multistate magnetization [34] and has also been demonstrated useful in optical nanoprobing [35]. Angular-momentum conversion is particularly valuable in multistate information encoding for quantum computing [36,37] and optical communication [38,39]. This kind of angular-momentum conversion processes are associated with the Pancharatnam-Berry phase induced by inhomogenous transformation of the polarization direction [40]. Therefore, inhomogeneous anisotropic medium becomes a reliable technique to achieve angular momentum conversion, such as q plate [38] and metasurface [41–43]. However, these elements achieve angular-momentum conversion with restricted direction and extremely rely on precisely designed geometric structures, which limit their applications especially considering many complex environments [44–47], such as under water, cloud and mist, sand and dust weather, etc. Therefore it is of fundamental relevance to realize the coherent control of spin and orbital angular-momentum conversion of light by a scattering system considering a variety of practical applications.

In these complex environments, the strong scattering effect of light in scattering media dominates. Such scattering media have chaotic and disordered internal structure,

*liuhaigang@sjtu.edu.cn

†xfchen@sjtu.edu.cn

‡These authors contributed equally to this work.

which randomly changes the original propagation and polarization direction of light [44]. Intuitively, the scattering effect of light is always regarded as the obstacle to the practical applications of light [44–47]. The information transition between different angular-momentum channels will be severely damaged by scattering media. From another perspective, the abundant optical processes in the scattering medium also make it a promising tool to achieve angular-momentum conversion under proper regulation [44]. According to previous investigation, there is a tight correspondence between the wave-front information of the incident light and the scattered light although the scattering system is chaotic [48]. Inspired by this, the feedback-based wave-front shaping (FBWS) method was proposed to handle this problem [49]. It combines the spatial light modulator (SLM) and mathematical algorithms [50,51] to achieve local optimal solution. As an effective tool to modulate the optical processes in scattering medium, FBWS has recorded many achievements such as focusing through scattering medium [49,52], noninvasive imaging [53], and nonlinear signal manipulation [54–56].

In this paper, we experimentally realize the active control of spin and orbital angular-momentum conversion of light by strongly scattering medium with the help of the FBWS method. Considering the coupling conversion control can be applied to identical degrees of freedom or between distinct degrees of freedom, we experimentally implement four classifications of angular-momentum conversion by scattering system, including the conversion of OAM-OAM, OAM-SAM, SAM-SAM, and SAM-OAM. The objective function in each conversion process obtains a significant increase and approaches a stable value with the operating of genetic evolution algorithm. The enhancement factor η, which is the ratio of the intensity at the detective region after optimization and the mean intensity of the scattering background, varies from 13 to 40 for different experiments over 200 generations of optimization. These repeatable and stable experimental results verify that the angular-momentum conversion process in scattering medium is flexible and tunable.

II. THEORETICAL ANALYSIS

Figure 1 describes the physical principle and schematic of the angular-momentum conversion process in scattering medium. The incident-light wave front on the SLM can be divided into $m \times n$ pixels with the same size, as shown in Fig. 1(a). The input light on each pixel is individually modulated by SLM and travels through the scattering medium along a specific path r. Different modulation phase in single modulation unit will change light path inside the scattering medium $(r, r', \ldots)$, which contribute different strength of angular-momentum conversion, as shown in Fig. 1(b). The input and output light on one pixel can be expressed as the quantum state and denoted as $|\phi\rangle_{m,n}$ and

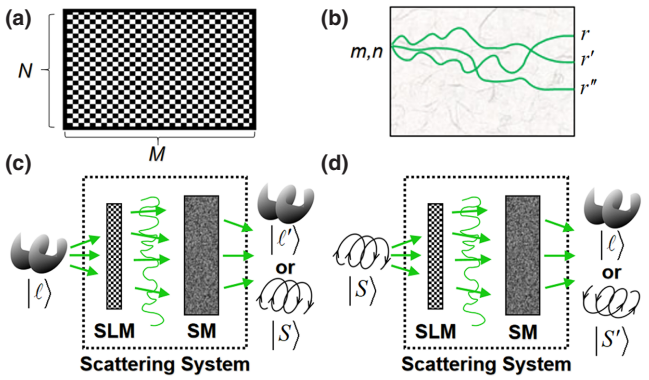

FIG. 1. Physical principle and schematic of the angular-momentum conversion process by scattering medium. (a) The modulation pixels on SLM, which can be divided into $m \times n$ units. (b) Different modulation phase in single pixel imposed by SLM will change light path inside the scattering medium $(r, r', \ldots)$, which contribute different strength of angular-momentum conversion. (c) Schematic of the coherent control of the conversion from OAM state to SAM state or different OAM states. (d) Schematic of the coherent control of the conversion from SAM state to different SAM states or OAM states. SLM, spatial light modulator. SM, scattering medium. $|\ell\rangle$, $|\ell'\rangle$, different OAM states. $|S\rangle$, $|S'\rangle$, left and right circularly polarized light with different SAM states, respectively.

$|\phi\rangle_{m,n}^{\text{out}}$, respectively. The input light states $|\varphi\rangle_{\text{input}}$ are the same as the light states on each pixels $|\phi\rangle_{m,n}$. After modulation of the SLM, they can be connected as the following formula:

$$|\phi\rangle_{m,n}^{\text{out}} = \hat{H}_{m,n}^{r} |\phi\rangle_{m,n}, \tag{1}$$

where the operator $\hat{H}_{m,n}^{r}$ means the SLM-controlled path operator determined by the phase modulation on the (m, n) pixel and scattering effect of path r. The optical state after the scattering medium is a combination of the states coming from all the pixels:

$$|\psi\rangle^{\text{out}} = \sum_{m,n} |\phi\rangle_{m,n}^{\text{out}} = \sum_{m,n} \hat{H}_{m,n}^{r} |\phi\rangle_{m,n}. \tag{2}$$

SLM modulates the wave-front state of light and changes the path into an alternative one r' for single pixel. Under this circumstance, the received optical state will also be transformed into an alternative $|\psi'\rangle^{\text{out}}$. After continuous optimization, we seek the optimal solution or the optimal phase modulation on the SLM to achieve the best angular-momentum conversion. It means that we can achieve coherent control of the angular-momentum conversion process within the scattering medium assisted by the FBWS.

As shown in Figs. 1(c) and 1(d), we present the schematic of the coherent control of angular-momentum conversion in scattering system based on the theory

described above. The incident light will be jointly influenced by the SLM modulation and the scattering effect of scattering medium, which is finally transformed into the target state being emitted from the other end of the scattering system through continuous optimization. The states of light at both ends of the scattering system can be flexibly changed, either polarized information carrying SAM or vortex phase carrying OAM.

III. EXPERIMENT

A. Conversion from OAM to SAM or OAM

In OAM-OAM experiment, the preset experiment goal here is the conversion of OAM with $\ell = 2$ to OAM with $\ell = 4,\ 6,\ 8,\ 10$ without loss of generality. The experimental setup is illustrated in Figs. 2(a) and 2(b). Figure 2(a) is the preparation of input OAM states. The light source is a cw laser with the wavelength of 532 nm. The polarization of laser beam is changed to horizontal direction by using the polarizer (P). The fundamental mode Gaussian laser beam is converted into vortex beam carrying OAM by passing through spiral phase plate (SPP_1, $\ell = 2$). The corresponding setup for modulation and detection of OAM after scattering is illustrated in Fig. 2(b). The SLM we use is a phase-only liquid crystal modulator (UPOLabs, HDSLM80R), which is only available for transversely polarized component of light, has a rate of 60 Hz, and a resolution of 1920×1200 pixels, each with a rectangular area of $8 \times 8\ \mu m^2$. We set a 20×20 pixel area as the modulation unit of the SLM mask. A smaller modulation unit obtains better optimization results but increases the optimization time. After modulation by SLM, the modulated beam is focused onto the scattering medium (SM) by L_1 ($f_1 = 100$ mm) and then collected by L_2 ($f_2 = 100$ mm). The scattering sample is $LiNbO_3$ powder deposited onto the glass substrate by electrophoresis method. The $LiNbO_3$ powder layer is about 100 μm thick, which is used to simulate strongly scattering environment. The output light passes through SPP_2 and L_3 ($f_3 = 200$ mm) and then is collected by a CMOS camera (DAHENG IMAGING, MER-U3), of which the response time is 1 ms. We implement 200 generations of optimization, which takes about 1 h. The reason for it is that the algorithm can converge and the optimization results can reach a stable threshold within 200 generations. SLM, L_1, L_2, and SPP_2 constitute a $4f$ system together. SLM and SPP_2 are, respectively, on the front focal plane of L_1 and the back front plane of L_2, which allows the phase modulation to be matched to SPP_2 for accurate detection of OAM [57]. In the experiment, the computer records the images on the camera and performs quantization analysis. In accordance with genetic algorithm (GA) [51], the optimization process is repeated until the objective function converges.

It is worth mentioning that we accomplish a calibration process to determine the target region in order to accurately detect the OAM state of output light. When the topological charge of the incident beam and SPP_2 match each other ($\ell_{OAM} = -\ell_{SPP}$), the phase singularity of the vortex beam will become a bright spot. These details are provided in Appendix A. In the experiment, we set the region of bright spot as the target region. The change of average light intensity in the target region reflects the corresponding OAM state intensity after the scattering medium.

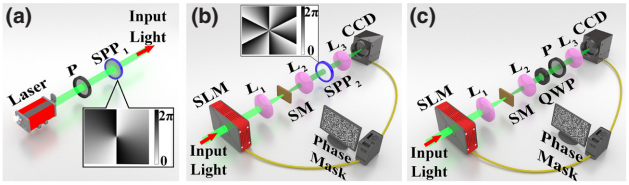

FIG. 2. Experimental setup for conversion from OAM to OAM or SAM. (a) The preparation of input light possessing different OAM states. (b) The modulation and detection system for OAM-OAM conversion. (c) The modulation and detection system for OAM-SAM conversion. P, polarizer; SPP_1, spiral phase plate with topological charge $\ell = 2$; BS, beam splitter; M, mirror; SM, scattering medium; SPP_2, spiral phase plate with different topological charges $\ell = -4, -6, -8, -10$; L_1–L_3, lens with focal length $f_{1-3} = 100, 100, 200$ mm; QWP, quarter-wavelength plate.

Figures 3(a)–3(d) and 3(i) are the experimental results for OAM-OAM conversion processes. The left images of Figs. 3(a)–3(d) are the intensity distribution of vortex beams carrying OAM with $\ell = 4,\ 6,\ 8,\ 10$. The middle images are the intensity distribution after different OAM light passing through the scattering medium before optimization. The red circles mark the target regions that we determine by the calibration process mentioned above. We set the intensity in target region as the objective function. The optimization results are shown in the right image of Figs. 3(a)–3(d). In the optimization process, the light intensity of the target region continually increases with the increasing of optimization generations. Finally, a very obvious bright spot appears in the target region, which means the output light has OAM of target topological charge. The corresponding intensity curves of target region with changing of generations are shown in Fig. 3(i). The curves of different colors represent the results of different target topological charges. It is clear that the light intensity of the target area keeps growing and eventually reaches convergence as the generation increases. The enhancement factor η reaches the value of about 16–20 after 200 generations. During the whole optimization process, the average intensity does not increase monotonically but in slight fluctuation, which is caused by the algorithm randomness. Overall, the intensity maintains the trend of increasing and achieves a local maximum value, which is consistent with the expectation. From the experimental results of Fig. 3(i), we can see that the enhancement factors do not

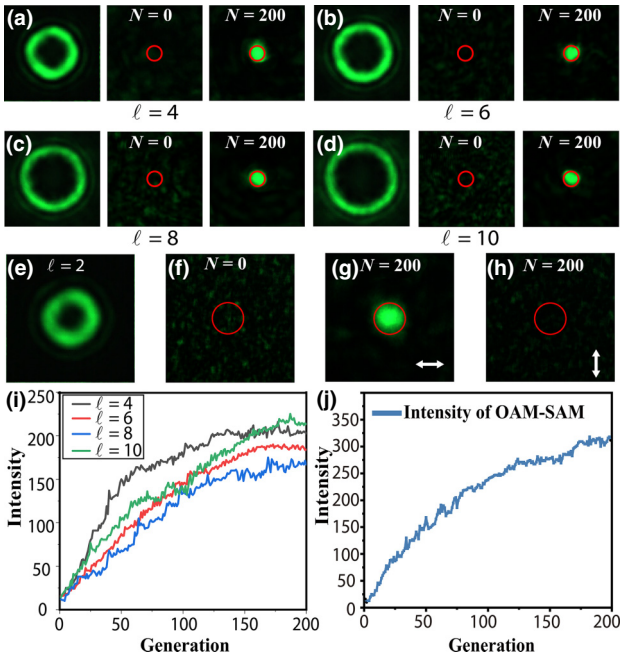

FIG. 3. Experimental results for conversion from OAM to OAM or SAM. (a)–(d), (i), Experimental results for OAM-OAM conversion. (a)–(d) are results of different topological charges $\ell = 4$, 6, 8, 10, respectively. In each group, the left image shows OAM state, the middle image shows intensity distribution of light after scattering. The right image shows intensity distribution of light after 200 generations optimization. The red circle indicates the optimization area determined by calibration process. (i) The curves of intensity varying with generations for different topological charges. The number of generations is 200. The enhance factor is about 16–20. (e)–(h) Experimental results for OAM-SAM conversion. (e) Intensity distribution of vortex beam with $\ell = 2$. (f) Intensity distribution of light captured by CCD after scattering. (g) Intensity distribution of light after 200 generations' optimization. (h) Intensity distribution after deflecting the optical axis of the polarizer to the vertical direction corresponding to the right circularly polarized light. (j) The curve of intensity varying with generations in OAM-SAM conversion. The optimization threshold is about 320. The enhance factor is about 40.

show significant correlation with the output OAM states because of the strongly scattering medium completely disrupting the wave-front information of the different OAM beams. Such a scattering effect is random and disorderly. Consequently, the role of different topological kernel components to angular-momentum conversion is averaged in such a stochastic process, which make the intensity curve basically irrelevant to the topological charge.

Figures 3(e)–3(h) and 3(j) show the experimental results for OAM-SAM conversion. The optical axis of the polarizer is preset to the horizontal direction corresponding to the left circularly polarized component of the scattered light. Figure 3(e) shows the intensity distribution of vortex beam produced by SPP_1 with $\ell = 2$. The intensity distributions of scattered light before and after optimization are, respectively, shown in Figs. 3(f) and 3(g). A bright green spot appears in the target area after optimization. The associated intensity growth curve is shown in Fig. 3(j). The average intensity continuously increases and eventually converges to a threshold value of 320. The enhancement factor is about 40. The above experimental results prove that the left circularly polarized component of the scattered light in the target region is significantly optimized and enhanced. In order to make the experimental results more rigorous, the optical axis of the polarizer is slowly adjusted to the vertical direction corresponding to the right circularly polarized component. As the optical axis shifts, the light spot in the target area gradually darkens and eventually becomes the speckle, as shown in Fig. 3(h). There is almost no bright green spot in the target area, which proves that the green spot obtained by the algorithm is almost the pure left circularly polarized light with SAM $= +\hbar$.

B. Conversion from SAM to SAM or OAM

The corresponding experimental setup for SAM-SAM conversion is illustrated in Figs. 4(a) and 4(b). Figure 4(a) is the state preparation of left circularly polarized light with SAM $= +\hbar$. The polarization of laser beam is firstly changed to horizontal direction by the polarizer and then adjusted to left circularly polarized light, which can be achieved by using the QWP_1 whose optical axis is 45° with respect to horizontal direction. The modulation and detection system for SAM-SAM conversion is shown in Fig. 4(b). The SLM used in our experiment is only sensitive to the transversely polarized component of light. Therefore, the QWP_2 before the SLM is used to convert left circularly polarized light to transversely polarized light, whose optical axis is 135° with respect to horizontal direction. After modulating by SLM, the modulated transversely polarized light changes back to phase-modulated left circularly polarized light by passing through the QWP_3 whose optical axis is 45° with respect to horizontal direction. This process is equivalent to spatial phase modulation to the light with SAM. After the scattering medium, the polarization state detection system is the same as the one in OAM-SAM experiment. With the help of FBWS, the scattered light is continuously optimized to the right circularly polarized light.

In this experiment, the circular area with a radius of 20 pixels at the center of the sparkle pattern as the target area. We set the average light intensity of this circular area as the objective function. Figures 5(a) and 5(b) show the intensity distribution received on the CCD before and after optimization, respectively. After 200 generations of the optimization process, a clear green bright spot appears in the target region. Such experimental results fit well with the intensity curve shown in Fig. 5(d). The growth curve of

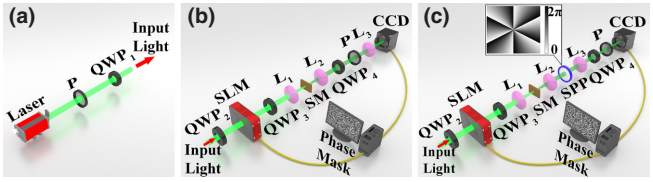

FIG. 4. Experimental setup for conversion from SAM to SAM or OAM. (a) The preparation of input SAM state with SAM $= +\hbar$. (b) The modulation and detection system for SAM-SAM conversion. (c) The modulation and detection system for SAM-OAM conversion. L_1–L_3, lens, $f_{1-3} = 100$, 100, 200 mm. SPP, spiral phase plate with $\ell = -2$. QWP_{1-4}, quarter-wavelength plate.

average light intensity maintains a steady overall growth while having local fluctuations and eventually converges to a threshold. The corresponding enhancement factor is about 23. Then the optical axis of the polarizer is rotated to the horizontal direction corresponding to the left circularly polarized component. As shown in Fig. 5(c), the green spot almost completely disappears, which indicates that the polarization direction of the scattered light is reversed.

The last optical process being controlled in our experiment is the spin-orbit interaction [58–61]. The

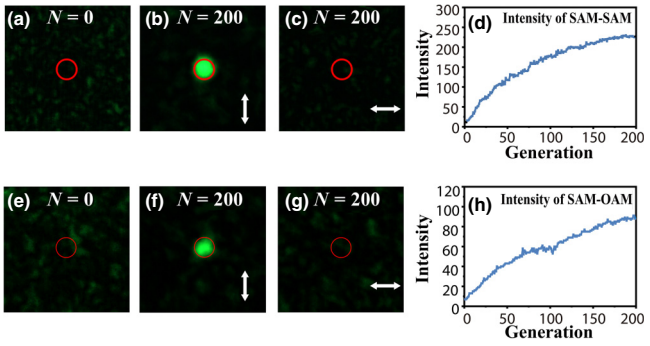

FIG. 5. Experimental results for conversion from SAM to SAM or OAM. (a)–(d), Experimental results for SAM-SAM conversion. (a) The intensity distribution captured by CCD after scattering medium. (b) The intensity distribution after 200 generations. (c) The intensity distribution after deflecting the optical axis of the polarizer to the horizontal direction corresponding to the left circularly polarized light. (d) The curve of intensity varying with the increasing of generations in SAM-SAM conversion. The light intensity finally reaches the value of 230 and the enhance factor is about 23. (e)–(h), Experimental results for SAM-OAM conversion. (e) Intensity distribution after scattering medium. (f) Intensity distribution after 200 generations of algorithm optimization. (g) Intensity distribution after deflecting the optical axis of the polarizer to the horizontal direction. The red circle indicates the target area to be optimized marked by the calibration. (h) The curve of intensity varying with the increasing of generations in SAM-OAM conversion. A typical intensity value is 91 after 200 generations and the enhance factor is about 13.

corresponding experimental setup is shown in Figs. 4(a) and 4(c). The input light is regulated to a left circularly polarized light and the output target light is a right circularly polarized vortex beam with a topological charge $\ell = 2$. The detection system shown in Fig. 4(c) achieves the detection of both polarization and OAM states. The SPP ($\ell = -2$) and L_3 are combined to detect the OAM component of beam while the QWP_4 and polarizer detect the right circularly polarization. In the process of OAM detection, calibration process is also required to determine the optimization target area, which is provided in the Appendix. In the experiment, we keep the SPP with topological charge of -2 and select light intensity of central target area as the feedback signal. Under such circumstances, the component of the scattered light carries both $-\hbar$ SAM and $2\hbar$ OAM is continuously enhanced.

The experimental results of SAM-OAM are shown in Figs. 5(e)–5(h). After the calibration process and determining the target area, we add the scattering medium to the light path and the scattered spot pattern is shown in Fig. 5(e). The optimization result is shown in Fig. 5(f) after 200 generations of genetic algorithm optimization. The light intensity in the target area corresponding to the right circularly polarized light has been significantly enhanced. Then we adjust the polarizer to the horizontal direction and the intensity distribution of light is shown in Fig. 5(g), in which the original bright green spot disappears. After active optimization and control of the scattering system, the scattered light is almost modulated into a right circularly polarized vortex light with $2\hbar$ OAM. Figure 5(h) is the curve of intensity varying with increasing of generations in SAM-OAM conversion. The intensity of target region obtains a relatively stable and continuous enhancement as the optimization process progresses. The corresponding enhancement factor is about 16. At the end of the optimization process, the growth rate of light intensity slows down significantly and the entire curve has obviously converged.

IV. DISCUSSION AND CONCLUSION

In SAM conversion experiment, we set the optimization target as pure polarized light in a local area rather than the overall polarization state of scattered light. In the practical application of using angular momentum as optical information carrier, it is common to modulate the polarization state of the beam in one channel. Therefore, it is more realistic to coherently regulate the polarization state of scattered light in a local region instead of the entire scattering plane. It is also indicated that the regulation of polarized light is not limited by the location of the target area and can be achieved in any channel. The coherently control of angular-momentum conversion of light by scattering system has useful applications prospects in the practical classical and quantum optical communication field. Compared

to previous elements, the angular-momentum conversion realized here has more flexible conversion directions, and is independent of precise geometry structure. These advantages originate from the full utilization of the disordered internal structure of scattering medium and the powerful coherent control of FBWS. Commonly, the information exchange between SAM and OAM in the complex environment will be severely limited by the scattering effect. Therefore, the method proposed here also effectively suppresses the negative effect of scattering on optical information exchange, which contributes to the development of high-dimensional optical information exchange in complex circumstance and non-line-of-sight high-dimensional optical communication [62] based on angular momentum.

The energy-conversion efficiency in our experiment is determined by measuring the power of the incident light and the target light. The typical conversion effect is about 2%. In our experiment, we use strongly scattering medium to simulate the scattering environment encountered. Therefore, the conversion efficiency is relatively low. Here, we just want to show that the method we propose is also feasible in such complex environment. In fact, such conversion efficiency can be improved by reducing the scattering intensity or the thickness of the scattering medium. Another issue is the sensitivity of our scattering system to lateral perturbation of the SM, which is estimated by the transmission matrix correlation theory called the generalized optical memory effect [63]. When the incident light reaching the scattering medium is tilted or laterally perturbed within a certain range, the scattering pattern remains constant except for tilting or having a laterally perturbation. The correlation function, which represents the correlation of the speckle pattern before and after the perturbation, is given by

$$C(\Delta r, \Delta k) = \exp\left(-\frac{L^3 k_0^2}{2\ell_{\mathrm{tr}}}\left[\frac{\Delta k^2}{3k_0^2} - \frac{\Delta k \cdot \Delta r}{k_0 L} + \frac{\Delta r^2}{L^2}\right]\right), \tag{3}$$

where L is the thickness of SM, ℓ_{tr} is the transport mean free path, Δk represents the changes in the direction of the wave vector, and Δr represents the lateral perturbation. In our experiment, L is 100 μm. As a simple estimate, ℓ_{tr} is shorter than L in consideration of the strong scattering effect of SM. Without considering the change in the direction ($\Delta k = 0$), the range of lateral perturbation distance that keeps the correlation function larger than $1/e$ is $\Delta r \leq \sqrt{2\ell_{\mathrm{tr}}/L}\Delta\lambda/2\pi \leq \sqrt{2}\lambda/2\pi = 0.12$ μm. Therefore, our scattering system is sensitive to the lateral perturbation.

In the practical applications of angular momentum in optical communications, the multiple input OAM states is necessary. Therefore, we implement the experiment of multiple OAM states' conversion by scattering. The details of the experiment are provided in Appendix B. We obtain significant optimization results, which demonstrate that our scattering system is valid to the conversion of multiple angular-momentum states.

We report the active control of interconversion of spin and orbital angular momentum of light by a scattering system with the help of FBWS. We explain theoretically how the angular-momentum conversion is controlled by FBWS in a scattering system. After hundreds of generations of optimization by FBWS, significant optimization results are obtained for each conversion process, which prove that the angular-momentum conversion by a scattering system is tunable and controllable. Besides, with the help of FBWS, the scattering system has the potential to become an alternative angular-momentum conversion element, which can effectively break through the limitations of previous elements including restricted conversion functions and highly demanding geometric structures. It also paves the way for the classical and quantum optical communication especially under complex environments where the scattering effect commonly destroys the optical information. Moreover, we realize the coupling control of not only one single degree of freedom but also different degrees of freedom in scattering medium. This kind of heterogeneous degree of freedom coupling can directly establish high-dimensional freedom optical channel conversion in a complex environment.

ACKNOWLEDGMENTS

We wish to acknowledge the support of National Key R&D Program of China (Grants No. 2018YFA0306301 and No. 2017YFA0303701); National Natural Science Foundation of China (NSFC) (Grants No. 12004245, No. 12192252, and No. 11734011); Shanghai Municipal Science and Technology Major Project (Grant No. 2019SHZDZX01-ZX06).

APPENDIX A: CALIBRATION PROCESS TO DETECT OAM

The OAM detecting system consists of SPP_2, L_3 and CCD. The calibration process in OAM-OAM conversion based on the interaction of vortex beam with SPP is shown in Fig. 6. From top to bottom are the processes of incident vortex beams with different topological charges. We use SLM to change topological charge of the light entering the detection system. The first column images show the intensity distribution of the vortex beam carrying OAM with $\ell = 4, 6, 8, 10$ in the absence of SPP_2. The other five images on the right are the far-field diffraction images when the OAM beam, respectively, passes through SPP_2 with different topological charges. It is obvious that the phase singularity at the center of the vortex beam changes after passing through SPP_2. Only when the topological charge of the incident beam and SPP_2 match ($\ell_{\mathrm{OAM}} = -\ell_{\mathrm{SPP}}$) each other, the phase singularity gets replaced by a bright spot. This property has been widely

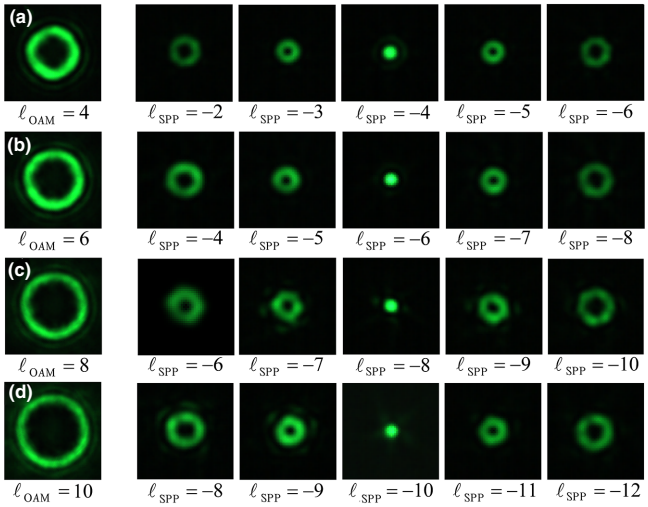

FIG. 6. Calibration processes of OAM-OAM conversion. (a)–(d) The calibration processes corresponding to different vortex beams with $\ell = 4, 6, 8, 10$ from top to bottom. The first column of the images is the intensity distribution of vortex beam produced by SLM. The right five images are far-field diffraction patterns of vortex beam passing through SPP_2 with different topological charges.

used in the detection of orbital angular momentum [57]. The region covered by the bright spot is the target region in the optimization algorithm.

Figure 7 shows the calibration in SAM-OAM conversion. Figure 7(a) shows the intensity distribution of the vortex beam with $\ell = 2$ produced by SLM. After adding SPP with different topological charges from -1 to -4, the intensity patterns on the CCD are shown in Figs. 7(b)–7(e), respectively. The target region for the optimization algorithm can then be determined from the variation of the phase singularity.

APPENDIX B: CONVERSION BETWEEN MULTIPLE OAM STATES

The preset experimental target is the conversion from the multiple OAM states with $\ell = 4$ and $\ell = 6$ to different multiple OAM states with $\ell = 2$ and $\ell = 8$. The corresponding experimental setup and results are illustrated in

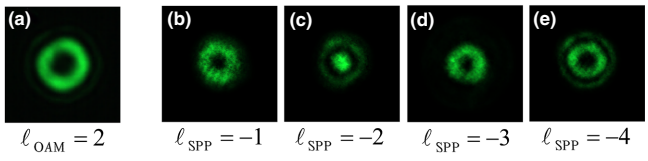

FIG. 7. Calibration process of SAM-OAM conversion. (a) The intensity distribution of vortex beam with $\ell = 2$ produced by SLM. (b)–(e) The far-field diffraction patterns after passing through SPP with different ℓ from -1 to -4.

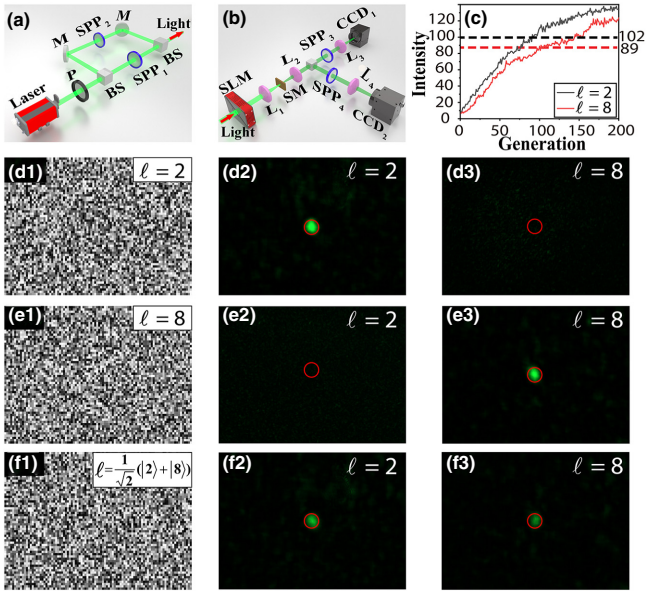

FIG. 8. Experimental setup and results for multiple OAM conversion. (a) The preparation of input light with multiple OAM states. (b) The modulation and detection system for multiple OAM conversion. $SPP_{1–4}$, spiral phase plate with $\ell = 4$, 6, -2, -8, respectively. (c) The intensity curves of target region with generations increasing corresponding to the conversions from multiple OAM states with $\ell = \left(1/\sqrt{2}\right)(|4\rangle + |6\rangle)$ to individual single OAM state with $\ell = 2$ or $\ell = 8$. The two dashed lines are the intensity of the target region obtained in the multiple OAM states conversion. (d)–(f) The experimental results of the conversion from $\ell = \left(1/\sqrt{2}\right)(|4\rangle + |6\rangle)$ to $\ell = 2$, $\ell = 8$, and $\ell = \left(1/\sqrt{2}\right)(|2\rangle + |8\rangle)$, respectively. (d1), (e1) and (f1) are the phase masks loaded to the SLM. (d2)–(d3), (e2)–(e3) and (f2)–(f3) are the intensity distribution on CCD_1 and CCD_2, respectively. The red circles mark the target regions.

Fig. 8. Figure 8(a) is the preparation of input multiple OAM states. The laser beam is split into two beams by BS. The two beams pass through different spiral phase plates SPP_1 ($\ell = 4$) and SPP_2 ($\ell = 6$) to obtain different OAM and form multiple OAM states by another BS. Figure 8(b) is the setup for modulation and detection of OAM after scattering. The scattering light is collected by L_2 and then split into two beams. Each of them passes through the same detection system, consisting of SPP, lens, and CCD, where SPP_3 has $\ell = -2$ and SPP_4 has $\ell = -8$. The principle of these devices is explained above.

The conversion between multiple OAM states is demonstrated by two processes. Firstly, the computer connects to CCD_1 and CCD_2, respectively, to realize two individual optimizations corresponding to conversion from multiple OAM states $\ell = \left(1/\sqrt{2}\right)(|4\rangle + |6\rangle)$ to single OAM state with $\ell = 2$ or $\ell = 8$. Each optimization has 200

generations and the target region on each CCD is determined by the calibration process. Figure 8(c) is the corresponding intensity curves of target region with changing of generations. The intensity keeps growing and eventually reaches convergence as the generation increases. The enhancement factor η reaches the value of 18 after 200 generations. Figures 8(d) and 8(e) are the experimental results of multiple-single OAM conversion with $\ell = 2$ and $\ell = 8$, respectively. Figures (d1) and (e1) are the phase masks after optimization loaded to the SLM. Figures 8(d2)–8(d3) and 8(e2)–8(e3) are the intensity distribution on CCD_1 ($\ell = 2$) and CCD_2 ($\ell = 8$), respectively. The red circles mark the target regions. It is obvious that in multiple-single OAM conversion, the optimized beam carries OAM with only one topological charge. Secondly, phase masks shown in Figs. 8(d1) and 8(e1) are used as the parents to generate new masks to realize multiple-multiple OAM conversion from $\ell = \left(1/\sqrt{2}\right)(|4\rangle + |6\rangle)$ to $\ell = \left(1/\sqrt{2}\right)(|2\rangle + |8\rangle)$. We load the new masks to SLM and filter out the best experimental results, which are illustrated in Figs. 8(f1)–8(f3). Figure 8(f1) is the filtered alternative phase mask and Figs. 8(f2)–8(f3) indicate that the optimized beam carries multiple OAM states with $\ell = \left(1/\sqrt{2}\right)(|2\rangle + |8\rangle)$. We want to point out that the light intensity in the red circle still exists when we block either of the incident OAM states. Compared to multiple-single OAM state conversion, the intensities of components with different OAM are both decreased. The corresponding intensities are illustrated in Fig. 8(c) as the two dashed lines. The enhancement factor η is reduced to the value of 13.

[1] J. H. Poynting, The wave motion of a revolving shaft, and a suggestion as AN angular momentum in a beam of circularly polarized beam, Proc. R. Soc. Lond. A **82**, 560 (1909).

[2] R. A. Beth, Mechanical detection and measurement of the angular momentum of light, Phys. Rev. **50**, 115 (1936).

[3] L. Allen, M. W. Beijersbergen, R. J. Spreeuw, and J. P. Woerdman, Orbital angular momentum of light and the transformation of Laguerre-Gaussian laser modes, Phys. Rev. A **45**, 8185 (1992).

[4] X. Ouyang, Y. Xu, M. Xian, Z. Feng, L. Zhu, Y. Cao, S. Lan, B. Guan, C. Qiu, M. Gu, and X. Li, Synthetic helical dichroism for six-dimensional optical orbital angular momentum multiplexing, Nat. Photonics **15**, 901 (2021).

[5] D. Naidoo, H. Sroor, Y. Huang, B. Sephton, A. Vallés, V. Ginis, Q. Zhan, C. Qiu, A. Ambrosio, F. Capasso, *et al.*, High-purity orbital angular momentum states from a visible metasurface laser,", Nat. Photonics **14**, 498 (2020).

[6] L. Chen, G. Zheng, J. Xu, B. Zhang, and W. She, Electrically controlled transfer of spin angular momentum of light in an optically active medium, Opt. Lett. **31**, 3474 (2006).

[7] R. René, D. Michael, H. Erik, R. Diehl, M. Frimmer, D. Windey, F. Tebbenjohanns, and L. Novotny, GHz Rotation of an Optically Trapped Nanoparticle in Vacuum, Phys. Rev. Lett. **121**, 033602 (2018).

[8] M. Friese, T. Nieminen, N. Heckenberg, and H. Rubinsztein-Dunlop, Optical alignment and spinning of laser-trapped microscopic particles, Nature **394**, 348 (1998).

[9] M. J. Padgett, Orbital angular momentum 25 years on [Invited], Opt. Express **25**, 11265 (2017).

[10] S. Franke-Arnold, L. Allen, and M. Padgett, Advances in optical angular momentum, Laser Photonics Rev. **2**, 299 (2008).

[11] G. Knöner, S. Parkin, T. A. Nieminen, V. L. Loke, N. R. Heckenberg, and H. Rubinsztein-Dunlop, Integrated optomechanical microelements, Opt. Express **15**, 5521 (2007).

[12] J. Courtial and M. J. Padgett, Limit to the orbital angular momentum per unit energy in a light beam that can be focussed onto a small particle, Opt. Commun. **173**, 269 (2000).

[13] D. G. Grier and Y. Roichman, Holographic optical trapping, Appl. Opt. **45**, 880 (2006).

[14] M. F. Picardi, K. Y. Bliokh, F. J. Rodríguez-Fortuño, F. Alpeggiani, and F. Nori, Angular momenta, helicity, and other properties of dielectric-fiber and metallic-wire modes, Optica **5**, 1016 (2018).

[15] N. B. Simpson, K. Dholakia, L. Allen, and M. J. Padgett, Mechanical equivalence of spin and orbital angular momentum of light: an optical spanner, Opt. Lett. **22**, 52 (1997).

[16] D. Gao, W. Ding, M. Nieto-Vesperinas, X. Ding, M. Rahman, T. Zhang, C. Lim, and C. Qiu, Optical manipulation from the microscale to the nanoscale: Fundamentals, advances and prospects, Light Sci. Appl. **6**, e17039 (2017).

[17] V. Garcés-Chávez, D. McGloin, M. J. Padgett, W. Dultz, H. Schmitzer, and K. Dholakia, Observation of the Transfer of the Local Angular Momentum Density of a Multiringed Light Beam to an Optically Trapped Particle, Phys. Rev. Lett. **91**, 093602 (2003).

[18] C. López-Mariscal, J. C. Gutiérrez-Vega, G. Milne, and K. Dholakia, Orbital angular momentum transfer in helical Mathieu beams, Opt. Express **14**, 4183 (2006).

[19] S. E. Olson, M. L. Terraciano, M. Bashkansky, and F. K. Fatemi, Cold-atom confinement in an all-optical dark ring trap, Phys. Rev. A **76**, 061404 (2007).

[20] G. Tkachenko, I. Toftul, C. Esporlas, A. Maimaiti, F. L. Kien, V. G. Truong, and S. N. Chormaic, Light-induced rotation of dielectric microparticles around an optical nanofiber, Optica **7**, 59 (2020).

[21] D. B. Ruffner and D. G. Grier, Optical Forces and Torques in Nonuniform Beams of Light, Phys. Rev. Lett. **108**, 173602 (2012).

[22] A. Mair, A. Vaziri, G. Weihs, and A. Zeilinger, Entanglement of the orbital angular momentum states of photons, Nature **412**, 313 (2001).

[23] R. Fickler, R. Lapkiewicz, W. Plick, N. Krenn, M. Schaeff, C. S. Ramelow, and A. Zeilinger, Quantum entanglement of high angular momenta, Science **338**, 640 (2012).

[24] S. S. R. Oemrawsingh, X. Ma, D. Voigt, A. Aiello, E. R. Eliel, G. W. 't Hooft, and J. P. Woerdman, Experimental

Demonstration of Fractional Orbital Angular Momentum Entanglement of Two Photons, Phys. Rev. Lett. **95**, 240501 (2005).

[25] R. Fickler, R. Lapkiewicz, M. Huber, M. Lavery, M. J. Padgett, and A. Zeilinger, Interface between path and orbital angular momentum entanglement for high-dimensional photonic quantum information, Nat. Commun. **5**, 4502 (2014).

[26] S. W. Hell and J. Wichmann, Breaking the diffraction resolution limit by stimulated emission: Stimulated-emission-depletion fluorescence microscopy, Opt. Lett. **19**, 780 (1994).

[27] J. Wang, J.-Y. Yang, I. M. Fazal, N. Ahmed, Y. Yan, H. Huang, Y. Ren, Y. Yue, S. Dolinar, M. Tur, and A. E. Willner, Terabit free-space data transmission employing orbital angular momentum multiplexing, Nat. Photonics **6**, 488 (2012).

[28] Z. Liu, S. Yan, H. Liu, and X. Chen, Superhigh-Resolution Recognition of Optical Vortex Modes Assisted by a Deep-Learning Method, Phys. Rev. Lett. **123**, 183902 (2019).

[29] J. Ni, C. Huang, L. Zhou, M. Gu, Q. Song, Y. Kivshar, and C. Qiu, Multidimensional phase singularities in nanophotonics, Science **374**, 418 (2021).

[30] N. Bozinovic, Y. Yue, Y. Ren, M. Tur, P. Kristensen, H. Huang, A. Willner, and S. Ramachandran, Terabit-scale orbital angular momentum mode division multiplexing in fibers, Science **340**, 1545 (2013).

[31] V. S. Liberman and B. Y. Zel'dovich, Spin-orbit interaction of a photon in an inhomogeneous medium, Phys. Rev. A **46**, 5199 (1992).

[32] S. Sukhov, V. Kajorndejnukul, A. Naraghi, and R. Dogariu, Dynamic consequences of optical spin–orbit interaction, Nat. Photonics **9**, 809 (2015).

[33] K. Y. Bliokh, F. J. Rodríguez-Fortuño, F. Nori, and A. V. Zayats, Spin-orbit interactions of light, Nat. Photonics **9**, 156 (2015).

[34] S. Lin, Z. Nie, W. Yan, Y. Liang, H. Lin, Q. Zhao, and B. Jia, All-optical vectorial control of multistate magnetization through anisotropy-mediated spin-orbit coupling, Nanophotonics **8**, 2177 (2019).

[35] O. G. Rodríguez-Herrera, D. Lara, K. Y. Bliokh, E. A. Ostrovskaya, and C. Dainty, Optical Nanoprobing via Spin-Orbit Interaction of Light, Phys. Rev. Lett. **104**, 253601 (2010).

[36] E. Nagali, D. Giovannini, L. Marrucci, S. Slussarenko, E. Santamato, and F. Sciarrino, Experimental Optimal Cloning of Four-Dimensional Quantum States of Photons, Phys. Rev. Lett. **105**, 073602 (2010).

[37] M. Erhard, R. Fickler, M. Krenn, and A. Zeilinger, Twisted photons: New quantum perspectives in high dimensions, Light Sci. Appl. **7**, 17146 (2018).

[38] L. Marrucci, C. Manzo, and D. Paparo, Optical Spin-to-Orbital Angular Momentum Conversion in Inhomogeneous Anisotropic Media, Phys. Rev. Lett. **96**, 163905 (2006).

[39] L. Marrucci, E. Karimi, S. Slussarenko, B. Piccirillo, E. Santamato, E. Nagali, and F. Sciarrino, Spin-to-orbital conversion of the angular momentum of light and its classical and quantum applications, J. Opt. **13**, 064001 (2011).

[40] G. Biener, A. Niv, V. Kleiner, and E. Hasman, Formation of helical beams by use of Pancharatnam–Berry phase optical elements, Opt. Lett. **27**, 1875 (2002).

[41] A. H. Dorrah, N. A. Rubin, M. Tamagnone, A. Zaidi, and F. Capasso, Structuring total angular momentum of light along the propagation direction with polarization-controlled meta-optics, Nat. Commun. **12**, 6249 (2021).

[42] T. Stav, A. Faerman, E. Maguid, D. Oren, V. Kleiner, E. Hasman, and M. Segev, Quantum entanglement of the spin and orbital angular momentum of photons using metamaterials, Science **361**, 1101 (2018).

[43] R. C. Devlin, A. Ambrosio, N. A. Rubin, J. P. B. Mueller, and F. Capasso, Arbitrary spin-to-orbital angular momentum conversion of light, Science **358**, 896 (2017).

[44] T. Bardon-brun, D. Delande, and N. Cherroret, Spin Hall Effect of Light in a Random Medium, Phys. Rev. Lett. **123**, 043901 (2019).

[45] V. Ntziachristos, Going deeper than microscopy: The optical imaging frontier in biology, Nat. Methods **7**, 603 (2010).

[46] A. F. Koenderink, A. Lagendijk, and W. L. Vos, Optical extinction due to intrinsic structural variations of photonic crystals, Phys. Rev. B **72**, 153102 (2005).

[47] A. Mosk, A. Lagendijk, G. Lerosey, and M. Fink, Controlling waves in space and time for imaging and focusing in complex media, Nat. Photonics **6**, 283 (2012).

[48] S. M. Popoff, G. Lerosey, R. Carminati, M. Fink, A. Boccara, and S. Gigan, Measuring the Transmission Matrix in Optics: An Approach to the Study and Control of Light Propagation in Disordered Media, Phys. Rev. Lett. **104**, 100601 (2010).

[49] I. M. Vellekoop and A. P. Mosk, Focusing coherent light through opaque strongly scattering media, Opt. Lett. **32**, 2309 (2007).

[50] I. M. Vellekoop and A. P. Mosk, Phase control algorithms for focusing light through turbid media, Opt. Commun. **281**, 3071 (2008).

[51] D. B. Conkey, A. N. Brown, A. M. Caravaca-Aguirre, and R. Piestun, Genetic algorithm optimization for focusing through turbid media in noisy environments, Opt. Express **20**, 4840 (2012).

[52] O. Katz, E. Small, Y. Bromberg, and Y. Silberberg, Focusing and compression of ultrashort pulses through scattering media, Nat. Photonics **5**, 372 (2011).

[53] J. Bertolotti, E. van Putten, C. Blum, A. Lagendijk, W. Vos, and A. Mosk, Non-invasive imaging through opaque scattering layers, Nature **491**, 232 (2012).

[54] Y. Qiao, Y. Peng, Y. Zheng, F. Ye, and X. Chen, Second-harmonic focusing by a nonlinear turbid medium via feedback-based wavefront shaping, Opt. Lett. **42**, 1895 (2017).

[55] H. Frostig, E. Small, A. Daniel, P. Oulevey, S. Derevyanko, and Y. Silberberg, Focusing light by wavefront shaping through disorder and nonlinearity, Optica **4**, 1073 (2017).

[56] O. Tzang, A. M. Caravaca-Aguirre, K. Wagner, and R. Piestun, Adaptive wavefront shaping for controlling nonlinear multimode interactions in optical fibres, Nat. Photonics **12**, 368 (2018).

[57] J. Jin, J. Luo, X. Zhang, H. Gao, X. Li, M. Pu, P. Gao, Z. Zhao, and X. Luo, Generation and detection of orbital angular momentum via metasurface, Sci. Rep. **6**, 24286 (2016).

[58] F. Cardano and L. Marrucci, Spin–orbit photonics, Nat. Photonics **9**, 776 (2015).

[59] G. Araneda, S. Walser, Y. Colombe, D. Higginbottom, J. Volz, R. Blatt, and A. Rauschenbeutel, Wavelength-scale errors in optical localization due to spin–orbit coupling of light, Nat. Phys. **15**, 17 (2019).

[60] X. Fang, H. Ren, and M. Gu, Orbital angular momentum holography for high-security encryption, Nat. Photonics **14**, 102 (2020).

[61] M. P. J. Lavery, F. C. Speirits, S. M. Barnett, and M. J. Padgett, Detection of a spinning object using light's orbital angular momentum, Science **341**, 537 (2013).

[62] Z. Liu, Y. Huang, H. Liu, and X. Chen, Non-line-of-sight optical communication based on orbital angular momentum, Opt. Lett. **46**, 5112 (2021).

[63] G. Osnabrugge, R. Horstmeyer, I. N. Papadopoulos, B. Judkewitz, and I. M. Vellekoop, Generalized optical memory effect, Optica **4**, 886 (2017).